

Large-scale Invasion Percolation with Trapping for Upscaling Capillary-Controlled Darcy-scale Flow

Hasan A. Nooruddin¹ · Martin J. Blunt¹

Received: 28 July 2017 / Accepted: 26 October 2017 / Published online: 28 November 2017
© The Author(s) 2017. This article is an open access publication

Abstract We apply steady-state capillary-controlled upscaling in heterogeneous environments. A phase may fail to form a connected path across a given domain at capillary equilibrium. Moreover, even if a continuous saturation path exists, some regions of the domain may produce disconnected clusters that do not contribute to the overall connectivity of the system. In such cases, conventional upscaling processes might not be accurate since identification and removal of these isolated clusters are extremely important to the global connectivity of the system and the stability of the numerical solvers. In this study, we address the impact of percolation during capillary-controlled displacements in heterogeneous porous media and present a comprehensive investigation using random absolute permeability fields, for water-wet, oil-wet and mixed-wet systems, where J-function scaling is used to relate capillary pressure, porosity and absolute permeabilities in each grid cell. Important information is revealed about the average connectivity of the phases and trapping at the Darcy scale due to capillary forces. We show that in oil-wet and mixed-wet media, large-scale trapping of oil controlled by variations in local capillary pressure may be more significant than the local trapping, controlled by pore-scale displacement.

Keywords Immiscible displacements · Capillary-driven flow · Large-scale percolation · Steady-state upscaling

List of symbols

A_p	Symmetric matrix used in percolation solver for a given phase
A_{ij}	Cross-sectional area between two nodes (m^2)
B	Adjacent matrix of a simulation model

✉ Hasan A. Nooruddin
h.nourdeen14@imperial.ac.uk

Martin J. Blunt
m.blunt@imperial.ac.uk

¹ Department of Earth Science and Engineering, Imperial College London, London, UK

B_{ij}	Element in row i and column j in matrix \mathbf{B} takes only a binary number
\mathbf{I}	Identity matrix
J	Leverett J-function (dimensionless)
\tilde{k}_{rp}^d	Average phase relative permeability in a given flow direction (fraction)
k_{rf}^c	Threshold value imposed at relative permeability to a fluid (fraction)
k_{ro}^{\max}	Maximum relative permeability to oil (fraction)
k_{rw}^{\max}	Maximum relative permeability to water (fraction)
k_b	Base permeability used in J-function calculations (m^2)
k_{ij}	Rock absolute permeability between two nodes (m^2)
k_{ro}	Relative permeability to oil (fraction)
k_{rp}	Relative permeability to a given phase (fraction)
k_{rw}	Relative permeability to water (fraction)
L_{ij}	Length between two nodes (m)
m^d	Total number of cross sections in averaged volume in direction d
N	Total number of grid cells
n_c^+	Capillary pressure exponent for $p_c(S_w) > 0$ (dimensionless)
n_c^-	Capillary pressure exponent for $p_c(S_w) < 0$ (dimensionless)
n_c^{dr}	Capillary pressure exponent for drainage (dimensionless)
n_o	Oil relative permeability exponent (dimensionless)
n_w	Water relative permeability exponent (dimensionless)
p_c^{level}	Array of capillary pressure levels, or equilibrium states (Pa)
p_c^{\max}	Array of maximum capillary pressure values (Pa)
p_c^{\min}	Array of minimum capillary pressure values (Pa)
p_c^{dr}	Capillary pressure for drainage (Pa)
p_c^{level}	Capillary pressure level, or equilibrium state (Pa)
p_c^{\max}	Maximum capillary pressure (Pa)
p_c^{\min}	Minimum capillary pressure (Pa)
p_c	Capillary pressure for waterflooding and imbibition (Pa)
p_e	Entry capillary pressure level (Pa)
P_p	Phase pressure (Pa)
P_s	Single-phase pressure (Pa)
\tilde{Q}^d	Average volumetric flux within a given volume in direction d (m^3/s)
$Q_{p\ell}$	Volumetric flux across a link ℓ between two neighbouring nodes (m^3/s)
\tilde{S}_{orw}	Average residual oil saturation (fraction)
\tilde{S}_{wir}	Average irreducible water saturation (fraction)
\tilde{S}_w	Average water saturation (fraction)
S^*	Water saturation at $p_c(S_w) = 0$ (fraction)
S_o^{trap}	Trapped oil saturation (fraction)
S_w^{trap}	Trapped water saturation (fraction)
S_w	Water saturation (fraction)
S_{orw}	Residual oil saturation (fraction)
S_{wir}	Irreducible water saturation (fraction)
V_b	Bulk volume (m^3)

Acronyms

MW	Mixed-wet
OW	Oil-wet

SWW	Strongly water-wet
WWW	Weakly water-wet

Greek Symbols

η_p	Fraction of invaded cells for a given phase
γ_p	Element of the phase mobility index takes only a binary number
Γ_p	Diagonal matrix with γ_p in its diagonal
$\boldsymbol{\gamma}_p$	Phase mobility index array takes only a binary number
λ_p	Phase mobility ($\text{Pa}^{-1} \cdot \text{s}^{-1}$)
λ_s	Single-phase mobility ($\text{Pa}^{-1} \cdot \text{s}^{-1}$)
μ_k	Mean of permeability distribution in normal domain (m^2)
μ_p	Phase viscosity (Pa.s)
μ_s	Single-phase viscosity (Pa.s)
$\mu_{\ln k}$	Mean of permeability distribution in logarithmic domain (m^2)
Ω_j	Set of links, or connections, intersecting the j -th cross-sectional area
ϕ	Rock porosity
ϕ_b	Base porosity used in J-function calculations
ψ_p^∞	Element of stationary distribution of invaded cells for a given phase
ψ_p	Element of the phase connectivity index takes only a binary number
Ψ_p^∞	Stationary distribution of invaded cells for a given phase
Ψ_p^0	Initial state of invaded cells for a given phase
Ψ_p^{k+1}	State of invaded cells at a new timestep
ψ_p	Phase connectivity index takes only a binary number
$\sigma_{\ln k}$	Standard deviation of permeability distribution in logarithmic domain (m^2)
σ_{wo}	Oil–water interfacial tension (N/m)
θ_{wo}	Oil–water contact angle (radians)
ξ_c	Percolation threshold
ξ_p	Fraction of open cells for a given phase

Subscripts

b	Bulk, or base depending on the context
c	Capillary
e	Entry
f	Fluid
i	Cell index
J	Index for cross-sectional area
ℓ	Link between two connected nodes
m	Trapped cell index
n	Last-cell index, equivalent to the number of cells in a simulation model
o	Oil
p	Phase
r	Relative
s	Single-phase
w	Water

Superscripts

d	Flow direction in one of the three main principal directions
dr	Drainage
k	Old timestep level in percolation algorithm
$k + 1$	New timestep level in percolation algorithm
level	Indicate the equilibrium level of variable
max	Indicate the maximum value of a variable
min	Indicate the minimum value of a variable
T	Transpose of an array
trap	Include trapping

1 Introduction

The flow of one or more fluids in porous rocks at the field scale is modelled using Darcy's law. Multiphase flow is represented by two functions of saturation: relative permeability and capillary pressure. Relative permeability is a dimensionless quantity, which indicates the average connectivity of a rock for a given phase when it partially saturates that rock (Muskat 1937). The capillary pressure, on the other hand, is the difference in pressure between two fluid phases at equilibrium (Leverett 1941). Although this definition of capillary pressure is precise at the pore scale at fluid–fluid interfaces, it becomes less accurate for large scales where the capillary pressure may be undefined once a phase loses its connectivity across a given domain. The capillary pressure will still be defined though at the pore scale at the interface of some disconnected fluid regions. For such cases, the corresponding relative permeability value for the disconnected phase is precisely zero, and only one phase is flowing inside that domain.

1.1 Importance of Upscaling

There are many experimental procedures used routinely in the industry to measure multiphase flow functions (Braun and Blackwell 1981; Johnson et al. 1959; Richardson et al. 1952; Osoba et al. 1951; Jones and Roszelle 1978); however, rock samples used are typically a few cm across, while the flow functions need to be input into reservoir simulation models with grid-block sizes of 10–100s m to predict flow at the km scale. In such cases, implementing an upscaling approach is required to capture the effects of sub-scale heterogeneities and the right balance of fluid forces into Darcy-scale simulations. Therefore, the main purpose of any upscaling process in porous media is to address two main factors as we increase the scale of investigation, the change in fluid forces and heterogeneity. The main fluid forces are viscous, capillary and gravitational forces. The relative importance of these forces varies depending on many parameters and strict separation between them may not be possible (Stephen et al. 2001; Hilden and Berg 2016). Nevertheless, it is usually observed that at relatively small scales capillary forces dominate the displacement process, while viscous and gravitational forces may become more important at larger scales (Odsæter et al. 2015; Kumar and Jerauld 1996; Jonoud and Jackson 2008a).

Numerous upscaling methods are available in the literature for two-phase flow (Guzman et al. 1999; Jacks et al. 1973; Kyte and Berry 1975; Stone 1991; Pickup and Sorbie 1996; Lohne et al. 2006; Virmovsky et al. 2004; King 1989; King et al. 1993; Coll et al. 2001; Wallstrom et al. 2002; Durlofsky 1997) among which flow-based methods are considered the

most reliable. Under this category, two fundamental approaches are employed: steady-state and dynamic pseudos. These methods are similar in concept to how multiphase flow properties are determined experimentally, but here numerical experiments are conducted. They also share the same strengths and weaknesses with their experimental counterparts (Honarpour and Mahmood 1988). Dynamic pseudo-functions are derived by performing a flow simulation in some region of a larger domain using a fine mesh and finding the average properties that reproduce the behaviour using a coarser simulation grid. In general, all dynamic pseudo-functions, produced at large scales, where viscous forces become important, depend on boundary conditions and the underlying gridding properties. They are only correct for the specific grid and flow conditions used to derive them (Barker and Thibeau 1997; Barker and Dupouy 1999).

1.2 Steady-state Upscaling

The main idea in steady-state upscaling is to estimate the distribution of fluid saturation and then apply a sequence of single-phase simulations for each phase individually to determine the effective multiphase flow functions. The process is repeated at different average saturations. Under specific conditions of flow, the method becomes computationally very efficient since it removes the need to run dynamic simulations for the fine-grid model. This is achieved through the assumption that only one force dominates the displacement process, while the other forces can be neglected. The term *capillary limit* is commonly used to describe capillary-dominated displacements, and *viscous limit* for viscous-dominated displacements. Gravitational forces are commonly neglected, since the method is applied to much smaller scales than those at which they become important. In general, the steady-state method gives more robust, stable and physically correct effective functions that do not depend on the details of the gridding and are less sensitive to the boundary conditions. The method could be in some cases computationally cheaper than dynamic pseudo-functions depending on flow conditions (Jonoud and Jackson 2008b, a). It becomes, however, very costly when the main fluid forces are considered in determining fluid distributions (Odsæter et al. 2015; Kumar and Jerauld 1996; Virmovsky et al. 2004; Stephen and Pickup 1999; Saad et al. 1995).

It is assumed under capillary-controlled displacements that viscous forces are negligible at the scale under investigation. This assumption only holds for regions that are away from saturation fronts, or for displacements with a large-scale capillary number that approaches zero.

Most implementations of capillary-controlled steady-state upscaling in the literature do not account for large-scale trapping since they do not permit complete disconnection of phases at the Darcy scale at a finite capillary pressure (Pickup and Stephen 1998; Ekrann and Aasen 2000). A few studies, however, have looked into this problem more carefully. Yortsos et al. (1991, 1993) considered large-scale percolation but for drainage only. They did include the effect of large-scale saturation trapping, demonstrating its importance for two-dimensional, 2D, uncorrelated media. Kueper and McWhorter (1992) introduced a macroscopic invasion percolation theory to upscale capillary pressure functions. They accounted for trapped cells using a percolation algorithm, but did not consider the impact on average saturation as a consequence of trapping inside these cells. In addition, the study did not compute average relative permeabilities and only considered 2D domains.

In this study, we focus on steady-state upscaling for capillary-controlled displacements, where we allow complete disconnection of phases at the Darcy scale, accounting for large-scale trapping of fluids. For this, large-scale invasion percolation is used as outlined by Kueper and McWhorter (1992) and Yortsos et al. (1991, 1993), but extended to waterflooding,

exploring the effects of wettability, while unambiguously accounting for large-scale fluid trapping inside trapped cells. This is illustrated using random permeability fields in 2D and 3D domains, correlated with local capillary pressure–saturation relationships using Leverett J-function scaling, assuming that heterogeneity in capillary pressure is connected primarily to heterogeneity in permeability and porosity. We also use characteristic J-function and local relative permeability curves that are typical for water-wet, oil-wet and mixed-wet systems.

We refer in this paper to the wetting phase as water and the non-wetting phase as oil, although the process is applicable to any pairs of immiscible fluids, including CO₂-brine systems where large-scale trapping is extremely important for storage security (Saadatpoor et al. 2010; Juanes et al. 2006).

2 Darcy-scale Saturation-Dependent Functions

Before going into the detail of large-scale trapping mechanisms, we define unambiguously large-scale saturation-dependent functions used in Darcy-scale simulations. Figure 1 shows typical capillary pressures and relative permeabilities for drainage and waterflooding. The main point here is that we do not allow the capillary pressure to diverge to infinity at end-point saturations: irreducible water S_{wir} and residual oil saturations S_{orw} . Instead, the functions are bounded by a maximum and a minimum value, p_c^{\max} and p_c^{\min} . To identify these points, the corresponding relative permeability functions are used, for when they are zero at the end-point saturations, the limits on the capillary pressure functions are well-defined. In this case, the phases are completely disconnected at the pore level, forming isolated clusters that are completely immobile.

In other cases, p_c^{\max} and p_c^{\min} may correspond to relative permeability values that are not zero but extremely small to the point that they can be considered immobile. Upon a closer look at the pore level, such a phase might be connected in thin layers (Valvatne and Blunt 2004). At larger scales, this layer flow might be neglected considering the timescale of the process (Blunt 2017). Here, a threshold value k_{fr}^c is imposed, below which layer flow is ignored. Having said this, there are no clear guidelines on how to find this cut-off value; it is case dependent. This will be investigated more thoroughly in future studies. In this study, we use a well-defined limits on capillary pressure functions, corresponding to zero relative permeabilities at end-point saturations.

If instead we only allowed the relative permeability to be zero at an infinite capillary pressure, then we would never disconnect phases in a steady-state simulation, since—for any finite imposed capillary pressure—the flow of both phases would be finite. We would then be unable to capture large-scale trapping; the residual saturation, regardless of heterogeneity, would be the residual saturation in the input relative permeability.

3 Theory of Large-scale Trapping of Fluids

There are two main trapping mechanisms that must be accounted for when calculating average fluid volumes and connectivities. These occur at the large scale and are distinct from the local trapping at the pore scale that is accounted for by end-point saturations in the local capillary pressures and relative permeabilities, mentioned above. The first mechanism is the trapping of *water* by *oil* during *drainage*. As oil invades the system at a given position of capillary equilibrium, referred to as p_c^{level} , some regions of the domain may trap some *movable* water

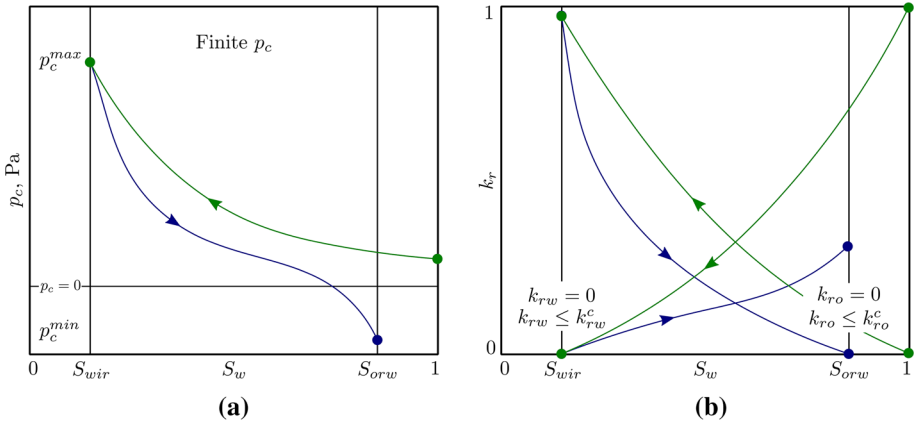


Fig. 1 A schematic of saturation-dependent functions defined at large scales. **a** Typical capillary pressures for drainage (green) and waterflooding (blue). **b** Typical relative permeabilities for drainage (green) and waterflooding (blue). Capillary pressures are bounded by p_c^{max} and p_c^{min} , corresponding to $k_{rf} = 0$, or $k_{rf} \leq k_{rf}^c$, for $f = \{o, w\}$

as *movable* water as *movable* oil fills completely neighbouring regions in which the relative permeability to water k_{rw} drops to zero. The trapped water volumes in these regions cannot be estimated from the local capillary pressure–saturation relationship $p_c(S_w)$ at a given p_c^{level} , as in conventional approaches, but rather a special treatment is required. Figure 2 demonstrates this trapping mechanism graphically in 2D systems, where the relevant cells are labelled from 1 to 5. Corresponding drainage capillary pressures are also shown in Fig. 2b. As fluids are brought to equilibrium at discrete, but elevated levels, water is trapped, *locally*, once p_c^{level} reaches p_c^{max} in a given cell. From the local capillary pressures in Fig. 2b, this local trapping of water takes place in the following order: cells 1,2,3 and 4. Large-scale trapping only happens when p_c^{level} reaches p_c^{max} of cell 4, at which the movable water in cell 5 becomes disconnected from the rest of the water in the system. As p_c^{level} increases above p_c^{max} of cell 4, S_w in cell 5 will remain fixed at S_w^{trap} , as indicated in Fig. 2b, and will not follow the local capillary pressure defined for that cell.

The second trapping mechanism is illustrated in Fig. 3. Here, oil is trapped by only-water-movable regions. The process occurs during *waterflooding*, in mixed-wet and oil-wet systems. As p_c^{level} decreases, the water saturation increases until, in some regions, the relative permeability to oil k_{ro} drops to zero, trapping movable oil in surrounded regions. This is shown in Fig. 3b where as p_c^{level} drops below p_c^{min} of cell 4, oil is trapped in cell 5 and stays fixed at S_w^{trap} as p_c^{level} continues to decline. The water saturation does not change in cell 5, since there cannot be any displacement of the trapped oil. In Fig. 3a, the arrangement of cells is shown in the 2D system, where blue indicates cells with local trapping of oil, while red indicates cells with large-scale trapping.

4 Steady-State Upscaling: Revised Procedure

In this section, we give a detailed description of the revised two-phase capillary-controlled steady-state upscaling method. In the capillary limit, it is assumed that fluids are distributed inside a region of interest in such a way that minimizes capillary pressure gradients. In

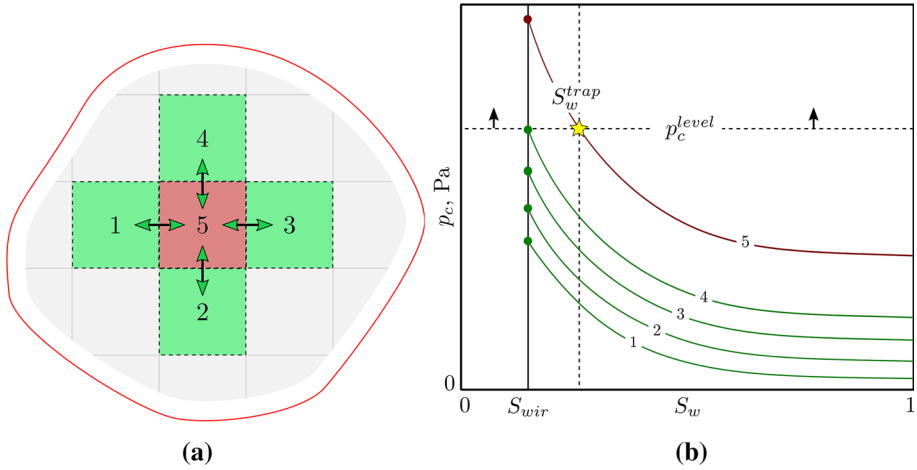


Fig. 2 An illustration of capillary trapping during *drainage* at the Darcy scale in 2D systems. **a** The arrangement of cells in the 2D system, showing their labels. Green indicates cells with local-scale trapping of water, while red indicates cells with large-scale trapping. **b** Corresponding local capillary pressure functions demonstrating the trapped water saturation S_w^{trap} in cell 5

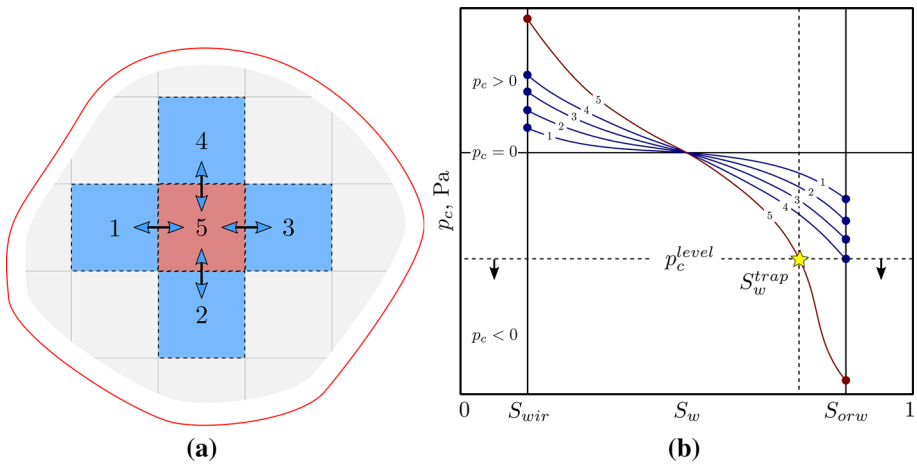
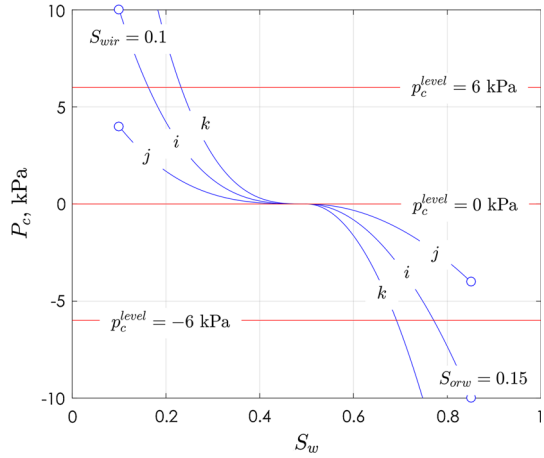


Fig. 3 An illustration of capillary trapping during *waterflooding* at the Darcy scale in 2D systems. **a** The arrangement of cells in the 2D system, showing their labels. Blue indicates cells with local-scale trapping of oil, while red indicates cells with large-scale trapping. **b** Corresponding local capillary pressure functions demonstrating the trapped water saturation S_w^{trap} in cell 5

the complete absence of other forces, capillary equilibrium is achieved when the gradient of capillary pressure approaches zero, resulting in a stationary distribution of fluids that is unique for the given set of initial and boundary conditions. At the Darcy scale, capillary equilibrium can be achieved by running a dynamic simulation for a given set of initial and boundary conditions until reaching a stationary fluid distribution. This is, however, a computationally very expensive procedure. A much more efficient and simpler way is to estimate the fluid distribution without running a dynamic simulation.

Fig. 4 Computations of S_w from waterflood $p_c(S_w)$ at three values of p_c^{level} in a system with three local capillary pressures labelled i, j and k . When $p_c^{level} = 6$ kPa, cell j does not allow water to move across it as the relative permeability to water is zero; only oil is mobile. At $p_c^{level} = 0$ kPa, both phases are mobile through all cells, whereas when $p_c^{level} = -6$ kPa, cell j becomes disconnected to oil as only water is allowed to move across it. In this last case, the relative permeability to oil is zero



The key idea is to use the local capillary pressure–saturation relationships that are already known at the grid-block scale and use them to estimate directly the saturation distributions. The main problem with this approach, which can be avoided by using dynamic simulations, is that fluid volumes required to achieve a certain capillary equilibrium state at a given local region might not be reached since there is no connected path for that fluid to flow to that region. In other words, a phase must make a connected path from inlet boundaries to the region of interest. From local relative permeability–saturation relationships, it is possible to identify these regions that do not allow a given phase to flow through them. This concept is illustrated graphically in Fig. 4, in which the water saturation distribution is estimated at three positions of p_c^{level} . The presented capillary pressures are typical for a waterflooding process in a mixed-wet system. When $p_c^{level} = 6$ kPa, cell j does not allow water to move across it as the relative permeability to water is zero; only oil is mobile. At $p_c^{level} = 0$ kPa, both phases are mobile through all cells, whereas when $p_c^{level} = -6$ kPa, cell j becomes disconnected to oil as only water is allowed to move across it. In this last case, the relative permeability to oil is zero.

The revised upscaling process then starts by assigning a capillary pressure level, p_c^{level} , at which capillary equilibrium is imposed for the connected phases in the domain. From local capillary pressure curves, the saturation distribution is estimated. The corresponding relative permeability values are also computed from local relative permeability curves, $k_{rp}(S_w)$ for $p = \{o, w\}$, and used to indicate whether a cell, or a node, can percolate a given phase across it or not. Once local non-percolating cells are identified, a solver that fills cells and determines whether a phase forms a connected cluster that spans the whole domain, is called; we refer to them as *invaded cells*. Such a condition confirms the presence of a global connectivity of the system. The solver is also used to identify cells that can percolate a given phase but could not be reached as a result of being locked in by neighbouring non-percolating cells. These are termed *trapped cells*, and they do not contribute to the overall connectivity of the system. In addition, special treatment is required to account for *the trapping of fluids* inside these *trapped cells*, as described previously in Sect. 3. Algorithms developed to tackle such problems are described next.

5 Filling Cells at a Given Capillary Pressure

In this section, we describe the algorithm used to determine invaded cells in a system. We simply describe how to invade cells for a given, specified capillary pressure. In the following section (Sect. 6), we describe how we account for trapping of fluids as the imposed capillary pressure is varied during a displacement. We here start by defining two main index functions, the *phase mobility* and the *phase connectivity* indices as detailed below, where subsequent calculations depend on both of them. We introduce a simple and efficient algorithm that works for structured and unstructured simulation grids.

5.1 Phase Mobility Index γ_p

The mobility index, γ_p , for a given phase, p , is an array defined as:

$$\gamma_p = [\gamma_{p_1}, \gamma_{p_2}, \dots, \gamma_{p_n}]^T, \tag{1}$$

where p refers to either oil, denoted as o , or water, denoted as w . The array has n elements equivalent to the number of cells in a simulation grid. The elements of γ_p are defined as follows:

$$\gamma_{w_i} = \begin{cases} 0, & p_{c_i}^{max} \leq p_c^{level}, \\ 1, & \text{otherwise,} \end{cases} \tag{2}$$

and,

$$\gamma_{o_i} = \begin{cases} 0, & p_{c_i}^{min} \geq p_c^{level}, \\ 1, & \text{otherwise.} \end{cases} \tag{3}$$

Equations 2 and 3 state that a cell i takes a value of 0 if a phase is immobile, otherwise the cell takes a value of 1. If the oil phase, for instance, is immobile for a given cell i , then $\gamma_{o_i} = 0$ for that cell, otherwise $\gamma_{o_i} = 1$. The index γ_p , therefore, is used to identify cells that have the ability to transmit a given phase and hence is termed the *phase mobility index*.

The process here represents a single step in a classic invasion percolation algorithm where γ_p indicates whether a phase can potentially flow across a given cell at a specified p_c^{level} or not (Kueper and McWhorter 1992; Yortsos et al. 1991, 1993; Hunt et al. 2014). The next step then is to use this mobility index to determine whether a given phase forms a connected path across a system or not. This is described below.

5.2 Phase Connectivity Index ψ_p

The phase connectivity index, ψ_p , for a given phase, p , is a vector defined as:

$$\psi_p = [\psi_{p_1}, \psi_{p_2}, \dots, \psi_{p_n}]^T, \quad p \in \{o, w\}, \tag{4}$$

where the subscript p refers to either oil, denoted as o , or water, denoted as w . The vector has n elements equivalent to the number of cells in the simulation model. The elements of ψ_p are either 0 or 1, where 1 indicates that a cell is invaded, otherwise it is not. The index function ψ_p , therefore, is used to indicate cells that are connected to the main cluster of a phase. The evolution of ψ_p with time is governed by

$$\psi_p^{k+1} = A_p \psi_p^k, \quad p \in \{o, w\}, \tag{5}$$

where the superscript k refers to the timestep number and A_p is a symmetric n -by- n matrix, given by

$$A_p = \Gamma_p (B + I) \Gamma_p, \quad p \in \{o, w\}, \tag{6}$$

where Γ_p is an n -by- n diagonal matrix having the vector γ_p in its diagonal, B is the adjacency matrix and I is the identity matrix. The adjacency matrix B is a square matrix in which the number of rows and columns is equal to the number of cells in a simulation model. The elements of this matrix are either 0 or 1, where 1 indicates that there is a connection, or a link, between a pair of cells (West 2001). More formally, the matrix can be constructed for any simulation model as follows:

$$B_{ij} = \begin{cases} 1, & \text{if cell } i \text{ is connected to cell } j, \\ 0, & \text{otherwise,} \end{cases} \tag{7}$$

where B_{ij} refers to the element in row i and column j of the matrix B .

The matrix Γ_p has the following structure:

$$\Gamma_p = \begin{pmatrix} \gamma_{p1} & & & \\ & \gamma_{p2} & & \\ & & \ddots & \\ & & & \gamma_{pn} \end{pmatrix}, \quad p \in \{o, w\}. \tag{8}$$

Equation 5 is a first-order difference equation that describes the evolution of invaded cells through a model. The process usually starts from one of the boundaries by providing an initial state of invaded cells, ψ_p^0 , where, as previously mentioned, the integer 1 indicates that a cell is invaded, while 0 indicates it is not. The invaded cells are then updated using Eq. 5. Because of the way the matrix A_p is defined in Eq. 6, at each iteration, ψ_p^{k+1} stores positive integer numbers which might be larger than one, indicating the number of possible visits to a given cell. For the purpose of our algorithm, all nonzero elements are reset to 1 at the end of each update. Iterations are then performed until the number of invaded cells does not change over time, at which the loop is terminated. This *stationary distribution of invaded cells* is referred to as ψ_p^∞ and is used in all subsequent calculations. In practice, the state of the cells at the far boundary from where the process has started are checked. If at least one of the cells has been invaded, $\psi_{pi}^\infty = 1$, then a given phase is said to have established a global connectivity across the system at the specified p_c^{level} . Calculations can then be performed to determine average relative permeabilities, where only invaded cells are taken into consideration. The overall algorithm for this filling process is shown in Fig. 5.

From the elements of γ_p and ψ_p^∞ , we calculate two important average quantities of the system. The first one is ξ_p , which describes the fraction of open cells, or cells that are accessible to a given phase. This parameter is particularly important in basic percolation theory, from which a critical fraction ξ_c is identified and used to indicate precisely when a global connectivity develops; it is universal for randomly disordered and infinitely large systems (Hunt et al. 2014; Grimmitt 1999). ξ_p can be calculated as

$$\xi_p = \frac{1}{N} \sum_{i=1}^n \gamma_{pi}, \quad p \in \{o, w\}, \tag{9}$$

where N is the total number of cells and γ_{pi} is the phase mobility index defined previously in Eqs. 1, 2 and 3.

The second quantity is η_p , which is defined as the fraction of invaded cells; it is given by

$$\eta_p = \frac{1}{N} \sum_{i=1}^n \psi_{pi}^\infty, \quad p \in \{o, w\}, \tag{10}$$

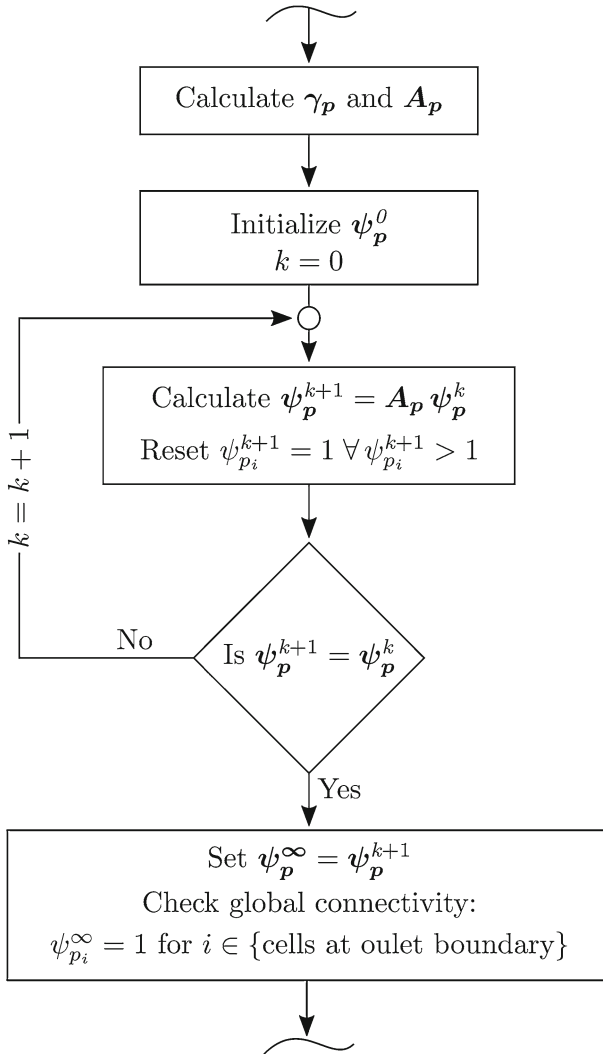


Fig. 5 A flowchart showing the algorithm for filling cells at a fixed p_c^{level} for both oil and water

where $\psi_{p_i}^\infty$ is the elements of the stationary distribution of invaded cells defined previously in Sect 5.2. These parameters will be used in Sect. 8 to validate the percolation solver for 2D and 3D systems.

6 Large-scale Invasion Percolation with Trapping

We now describe our large-scale invasion percolation algorithm that accounts for large-scale saturation trapping. In the previous section, we showed how to fill cells—finding invaded cells—at a given p_c^{level} , but here we allow p_c^{level} to vary between different equi-

librium positions. We also show how we determine the saturation distribution at each p_c^{level} , while accounting for fluid trapping.

A flowchart that illustrates this is shown in Fig. 6. We start first by determining the p_c^{level} distribution in which the events of trapping are represented by its elements, $p_{c_j}^{level}$. This distribution can be estimated either from p_c^{max} for drainage, or from p_c^{min} for waterflooding, corresponding for maximum and minimum capillary pressure distributions, respectively. This will be explained more in Sect. 9 when we show our examples.

Before iterating on $p_{c_j}^{level}$, p_c^{level} is sorted either in descending or in ascending order, depending on the displacement process being modelled. In waterflooding, for instance, the distribution is sorted in descending order, resembling the process for steady-state experiments, in which capillary pressure is brought to equilibrium in discrete levels from a higher to a lower equilibrium state. On the other hand, the distribution for drainage is sorted in ascending order as capillary equilibrium rises incrementally. Then, we initialize an array, p_c^{trap} , to store the capillary pressure levels, or events, at which trapping happens in each cell. The length of this array is equivalent to the number of cells N in the model. p_c^{trap} is initialized to zero, indicating that all cells are initially not trapped.

We then start the iterations at a given $p_{c_j}^{level}$, from which the mobility indices, γ_w and γ_o , are computed as in Eqs. 2 and 3. After that, the solver described in Fig. 5 is called to determine the stationary distribution of invaded cells, ψ_p^∞ . At the *current* position of $p_{c_j}^{level}$, trapped cells m are identified as those that allow a phase to move across them ($\gamma_{pm} = 1$), but have not been invaded at the current event ($\psi_{pm}^\infty = 0$), giving that they have not been trapped from previous events ($p_{c_m}^{trap} = 0$). This is a crucial step in the process since we need to find the *new* trapped cells at the *large scale* and at the *current* $p_{c_j}^{level}$. These conditions represent the trapping mechanisms as detailed in Sect. 3. We also exclude cells with ($\gamma_{pm} = 0$) as they represent cells with local trapping.

The trapped cells m are assigned then to the current $p_{c_j}^{level}$ where this value will stay constant. This condition is stated in Fig. 6 in set-builder notation. The average water saturation \tilde{S}_w can then be calculated at the end of each iteration, as follows

$$\tilde{S}_w = \frac{\sum_{i=1}^n \phi_i V_{b_i} S_{w_i}}{\sum_{i=1}^n \phi_i V_{b_i}}, \tag{11}$$

where ϕ_i is the porosity, V_{b_i} is the bulk volume in m^3 , and S_{w_i} is the water saturation of cell i determined inversely from local $p_{c_i}(S_w)$, where $p_{c_j}^{level}$ is used for non-trapped cells ($p_{c_i}^{trap} = 0$), and *nonzero* elements of p_c^{trap} are used for trapped cells.

7 Average Relative Permeability Algorithm

The computation of average relative permeability is described by a flowchart in Fig. 7. At a given capillary equilibrium state, ξ_p is computed and checked. When $\xi_p \neq 1$, this indicates that some cells with local trapping are present which might produce some large-scale trapping regions. In this case, a percolation solver is called to confirm global connectivity of a phase. Once confirmed, a flow solver is called to calculate \tilde{k}_{rp}^d using Eq. 12. The key step here is to remove the trapped cells at both the local and the large scales from the main matrix, since

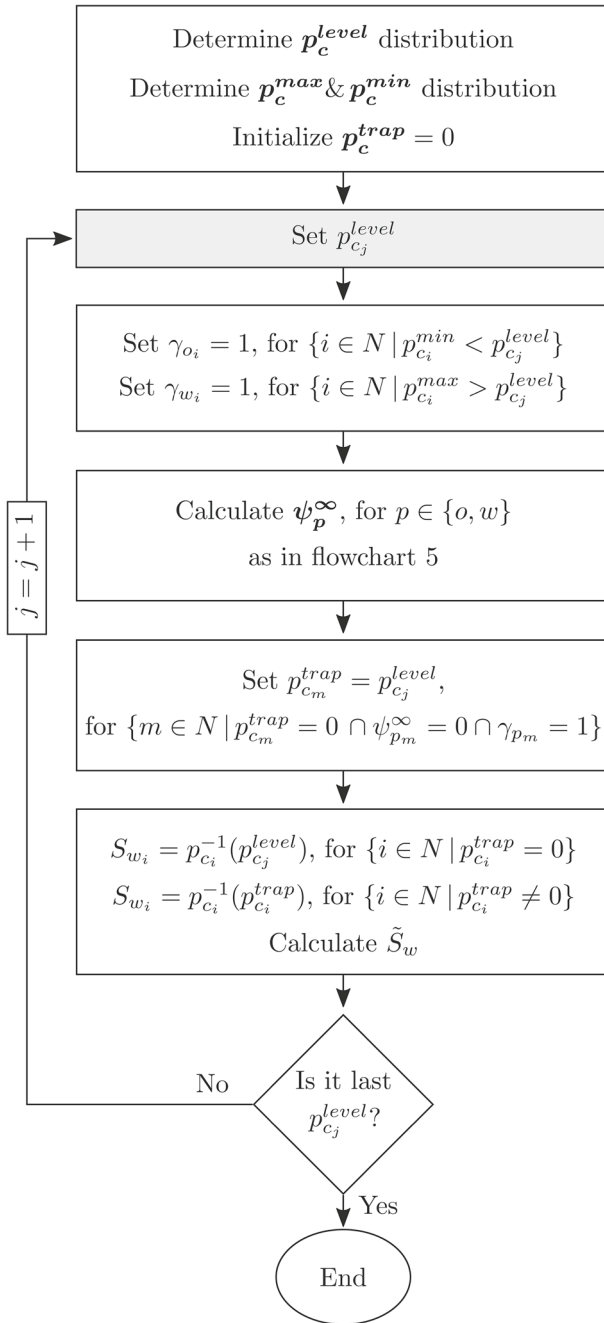


Fig. 6 A flowchart illustrating the algorithm for macroscopic invasion percolation where p_c^{level} is varied. This also shows the computations of average fluid saturation at each p_c^{level} accounting for fluid trapping for both oil and water

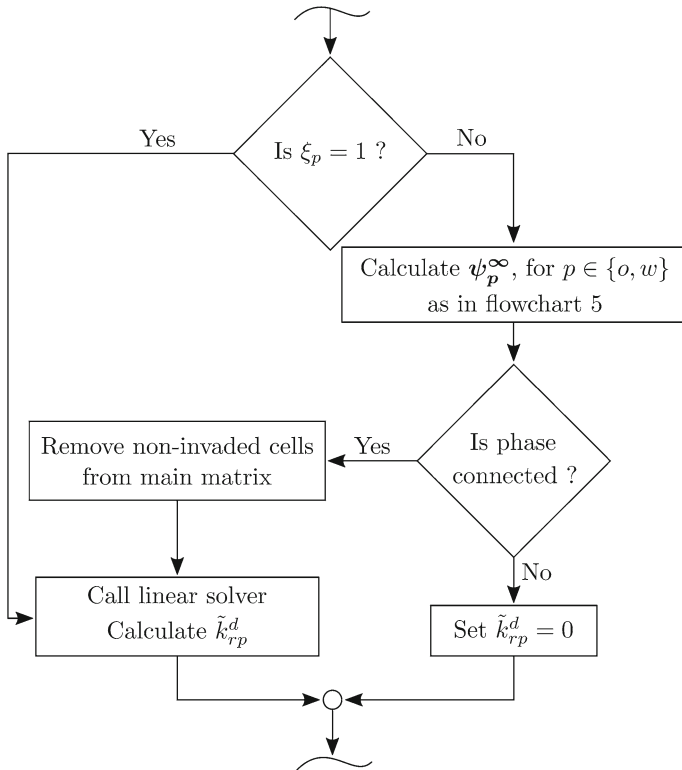


Fig. 7 A flowchart demonstrating the computations of average relative permeabilities for oil and water, considering the impact of invasion percolation with trapping

they do not contribute to the flow, and their inclusion could make the matrix ill-conditioned or even singular.

The average relative permeabilities are computed from:

$$\tilde{k}_{rp}^d = \frac{\mu_p}{\mu_s} \frac{\tilde{Q}_p^d}{\tilde{Q}_s^d}, \quad p \in \{o, w\}, \quad d \in \{x, y, z\}, \tag{12}$$

where \tilde{k}_{rp}^d is defined as the average relative permeability for a phase p in the direction d parallel to one of the coordinate axes of the three-dimensional system, μ_p is the phase viscosity in Pa.s and μ_s is the fluid viscosity used in single-phase calculations. The parameter \tilde{Q}^d is the average volumetric flux within a volume of interest in a direction d in m^3/s . The subscripts p and s are used to indicate whether the volumetric flux is obtained from two-phase or single-phase flow calculations, respectively. Both functions, $\tilde{Q}_{p,s}^d$, can be computed from numerical simulations as follows:

$$\tilde{Q}_{p,s}^d = \frac{1}{m^d} \sum_{j=1}^{m^d} \sum_{\ell \in \Omega_j} Q_{\{p,s\}\ell}, \quad p \in \{o, w\}, \quad d \in \{x, y, z\}, \tag{13}$$

where m^d is the total number of cross-sectional areas in the averaged volume perpendicular to a flow in direction d , $Q_{p\ell}$ is a volumetric flux across a link ℓ between two neighbouring

nodes in m^3/s and Ω_j here indicates the set of links, or connections, intersecting the j -th cross-sectional area. The way to use Eq. 13 to compute *average* flow rates is, therefore, to first calculate *total* flow rates across each cross-sectional area and then to average them out. If we allow, for instance, a flow along the x-axis in a 3D system with a cubic grid, we first sum the fluxes from the cells intersecting a single plane in the y–z direction. We record this value and repeat the process in all other parallel planes. The number of planes in this case is equivalent to m^d . We then average these fluxes as shown in Eq. 13.

Similarly for \tilde{Q}_s^d , average volumetric flux for single-phase flow, the calculations are performed as with \tilde{Q}_p^d in Eq. 13. The only difference is in the definition of the volumetric flux $Q_{p,s}$ across any pair of nodes i and j . This is given by the multiphase Darcy equation:

$$Q_{\{p,s\}ij} = \frac{k_{ij} A_{ij}}{L_{ij}} \lambda_{\{p,s\}ij} (P_{\{p,s\}i} - P_{\{p,s\}j}), \quad p \in \{o, w\}, \tag{14}$$

where k_{ij} is the absolute permeability of the link in m^2 , which is calculated as the harmonic mean of the absolute permeability of the nodes i and j : $\left(\frac{2k_i k_j}{k_i + k_j}\right)$, A_{ij} is the cross-sectional area between the two nodes in m^2 , L_{ij} is the length between them in m , and $\lambda_{p_{ij}}$ is the phase mobility defined as, for two-phase flow $\lambda_{p_{ij}} = \frac{k_{rp}(S_{w_{ij}})}{\mu_p}$, while for single-phase flow it is given by $\lambda_{s_i} = \mu_s^{-1}$. The phase mobility in two-phase flow is calculated from individual nodes as $\lambda_{p_{ij}} = \frac{f}{2} (\lambda_{p_i} + \lambda_{p_j})$, given that the saturation distribution is already known as previously described in Sect. 4. In Eq. 14, $P_{\{p,s\}}$ is the phase pressure in Pa for two-phase P_p or single-phase P_s flow calculations. They are determined by solving a system of equations constructed by applying material-balance principles, from which we obtain: $\sum_j Q_{\{p,s\}ij} = 0$.

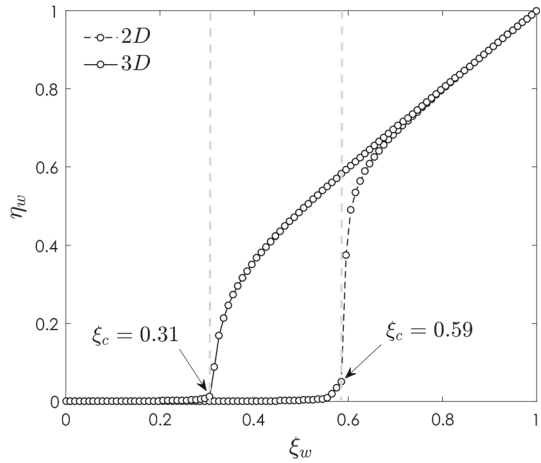
For the calculation of average relative permeabilities, it is important to apply the same set of boundary conditions for pressure when solving for P_p and P_s . In our solution, a pressure boundary condition is applied uniformly across inlet and outlet boundaries in one flow direction while other boundaries are kept closed. We find the average relative permeabilities for the whole computational domain. It should be also noted that μ_s can be arbitrary chosen with no impact on the average permeabilities, as long as Eq. 12 is strictly followed; this is also true for the magnitude of pressure drop applied at the boundaries of the system.

8 Validation

We here validate our percolation solver described previously in Sects. 5 and 6, by using a 2D model with a square grid and a 3D model with cubic grid blocks. The process simulated here is mainly for validation purposes and does not represent either conventional drainage or waterflooding. The main idea is to compute, using our solver, the site percolation thresholds and compare them to estimates from the literature of percolation theory. This only involves identifying trapped cells without accounting for trapped fluids inside them.

We use 1000×1000 grid cells for the 2D model, while $200 \times 200 \times 200$ grid cells are used for the 3D case. Figure 8 demonstrates the results, in which the fraction of invaded cells for an invading phase, η_w is plotted against the fraction of open cells for the invading phase, ξ_w . The percolation threshold ξ_c is estimated at 0.59 and 0.31 in 2D and 3D systems, respectively. These values are determined here precisely from the steady-state distribution of invaded cells ψ_w^∞ at the far boundary, as detailed in Sect. 5. From percolation theory for site percolation, $\xi_c = 0.5927$ in a 2D square lattice (Jacobsen 2015; Newman and Ziff 2000;

Fig. 8 Fraction of invaded cells, η_w against fraction of open cells, ξ_w for 2D and 3D systems. For the 2D case, 1000×1000 grid cells have been used to produce the results, while using $200 \times 200 \times 200$ grid cells for the 3D case. The percolation threshold, ξ_c , is estimated from this plot at 0.59 and 0.31 for site percolation on the 2D square lattice and the 3D simple cubic lattice, respectively. ξ_c is indicated in the plot by the sudden jump in η_w , which is very clear in 2D while being less obvious in 3D



Lee 2007), and $\xi_c = 0.3116$ in a 3D simple cubic lattice (Xu et al. 2014; Škvor and Nezbeda 2009; Deng and Blöte 2005), which closely matches results obtained from our simulations. Higher accuracy can be achieved by increasing the number of grid cells and applying a very small step size in ξ_w .

Results, as shown in Fig. 8, indicate a strong correlation between the percolation threshold, ξ_c , and the dimensionality of the model. This is usually expressed in terms of the coordination number; the number of nearest neighbouring grid cells, being 4 in the 2D and 6 in the 3D models used here. As the coordination number increases, the percolation threshold decreases, making lattice representation for macroscopic percolations a very critical issue for 2D and 3D models, since they can be represented with different combinations of coordination numbers. For this, it is not obvious which coordination number should be used for a valid representation of a heterogeneous system. Nevertheless, it has been shown that these sensitivities to coordination number become less important in spatially correlated media, where cells with similar properties are clustered together (Ioannidis et al. 1993, 1996). Hence, it is less likely to have an accessible cell neighbouring a trapped cell. This, however, depends on the correlation length of the system under investigation (Ioannidis et al. 1996).

Figure 9 shows spatial distributions of γ_w and ψ_w^∞ for the 2D system at different values of ξ_w . The process starts from the left face in the horizontal direction, while boundaries on the vertical direction are closed. Blue here represents cells in which an invading phase resides (invaded cells), while other cells are trapped. These trapped regions contain two types of cell: (1) cells with local trapping of the invading phase (green), and (2) cells that are accessible by the invading phase but are trapped at the large scale as being locked in by the green cells (grey).

Figure 9a shows the stationary distribution at $\eta_w = 2.64\%$ and $\xi_w = 57.52\%$, where no global connectivity is observed. In Fig. 9b, simulations are shown for just below ξ_c at $\eta_w = 19.05\%$ and $\xi_w = 59.32\%$. Figure 9c indicates invasion percolation just above ξ_c at $\eta_w = 41.53\%$ and $\xi_w = 59.42\%$. Lastly, Fig. 9d shows stationary distributions at $\eta_w = 50.15\%$ and $\xi_w = 60.51\%$, above ξ_c .

Similarly for the simple cubic model, Fig. 10 depicts large-scale invasion percolation in a 3D system. The invading phase is allowed to enter the system from one end while the opposite end is left open. The other boundaries are closed. Invaded cells are coloured based on their distance from the inlet boundary. Other cells are not displayed. Figure 10a shows

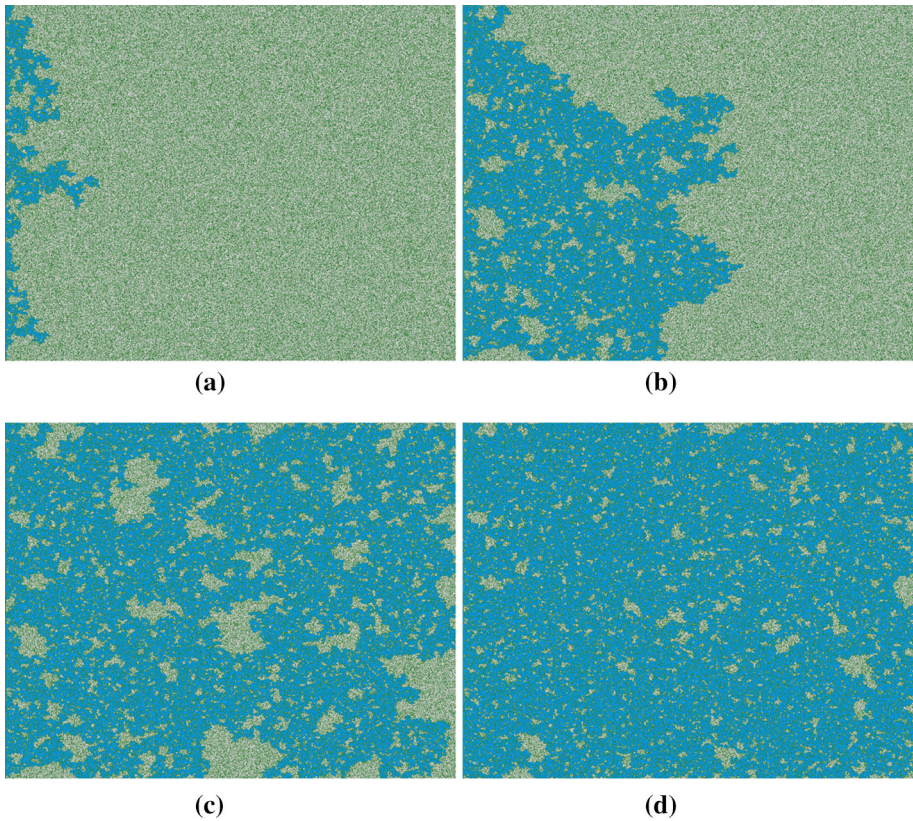


Fig. 9 Site percolation on a square lattice consisting of 1000×1000 grid cells. The process starts from the left face in the horizontal direction, while boundaries on the vertical direction are closed. Blue represents invaded cells while other cells are trapped. The trapped regions contain two types of cells: (1) green cells indicating that they do not percolate the invading phase across them (local trapping of the invading phase) and (2) grey cells representing cells with large-scale trapping; they are accessible by the invading phase but are surrounded by green cells. **a** The stationary distribution of invaded cells (blue) at a given capillary equilibrium state below the percolation threshold where there is no global connectivity ($\eta_w = 2.64\%$, $\xi_w = 57.52\%$). **b** The fluid distribution just below ξ_c at $\eta_w = 19.05\%$ and $\xi_w = 59.32\%$. **c** Invasion percolation just above ξ_c at $\eta_w = 41.53\%$ and $\xi_w = 59.42\%$. **d** The distribution for at $\eta_w = 50.15\%$ and $\xi_w = 60.51\%$

the stationary distribution of invaded cells below ξ_c at $\eta_w = 1.68\%$, $\xi_w = 30.70\%$, whereas Fig. 10b displays simulation just below ξ_c at $\eta_w = 2.50\%$ and $\xi_w = 30.89\%$. In Fig. 10c, invasion percolation just above ξ_c at $\eta_w = 4.48\%$ and $\xi_w = 31.13\%$ is demonstrated. Figure 10d shows stationary distributions at $\eta_w = 6.74\%$ and $\xi_w = 31.36\%$, well above ξ_c .

9 Illustrative Examples

We present here an example solution using our large-scale invasion percolation algorithm coupled with a Darcy-scale solver. We do not consider hysteresis in the capillary pressure and relative permeability: locally trapped saturations are not allowed to change with initial

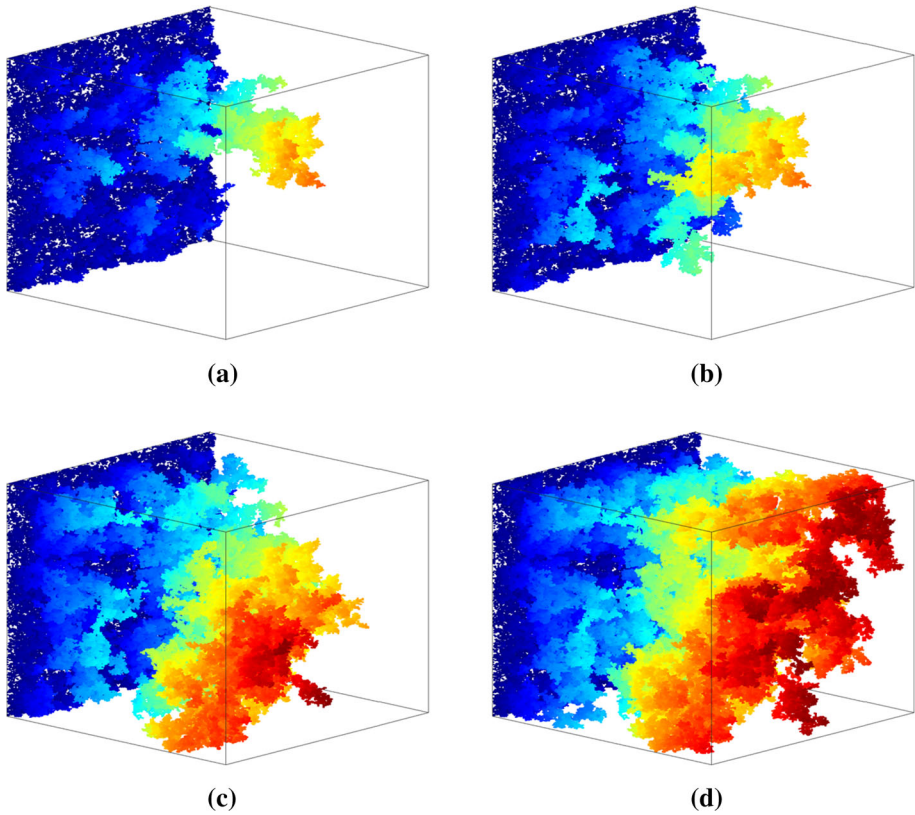


Fig. 10 Invasion percolation on a simple cubic lattice with $200 \times 200 \times 200$ grid cells. Two opposite boundary faces are open, while the other faces are closed. Coloured cells represent the stationary distribution of invaded cells at a given capillary equilibrium state. The change in colours indicates distance from inlet (blue being close to the inlet boundary). **a** The stationary distribution of invaded cells below ξ_c at $\eta_w = 1.68\%$, $\xi_w = 30.70\%$. **b** The distribution just below ξ_c at $\eta_w = 2.50\%$ and $\xi_w = 30.89\%$. **c** Invasion percolation just above ξ_c at $\eta_w = 4.48\%$ and $\xi_w = 31.13\%$. **d** The distributions for $\eta_w = 6.74\%$ and $\xi_w = 31.36\%$

saturation. This will be a topic for future work. For our simulations, we use two models: a 2D with 1000×1000 grid cells, and another a 3D model with $200 \times 200 \times 200$ grid cells.

We use synthetic data representing four different wettability states: strongly water-wet (SWW), weakly water-wet (WWW), mixed-wet (MW) and oil-wet (OW). For each wetting state, absolute permeability is randomly distributed from an uncorrelated log-normal distribution with a known mean and standard deviation. The mean is kept fixed in all simulations at $\mu_{lnk} = -29.9336$, equivalent to $\mu_k = 1 \times 10^{-13} \text{ m}^2$, while the standard deviation varies over two sets of values $\sigma_{lnk} = \{1, 2\}$. Porosity is kept constant at $\phi = 0.25$.

For the modelling of multiphase flow functions, the following mathematical expressions are used:

$$p_c^{dr}(S_w) = \begin{cases} (p_c^{\max} - p_e) \left(1 - \frac{S_w - S_{wir}}{1 - S_{wir}}\right)^{n_c^{dr}} + p_e, & S_w \in [S_{wir}, 1] \\ \emptyset, & S_w \notin [S_{wir}, 1] \end{cases} \quad (15)$$

Table 1 Parameters used to generate relative permeability and capillary pressure data in the Illustrative Examples section

	Strongly water-wet	Weakly water-wet	Mixed-wet	Oil-wet
S_{wir}	0.1	0.1	0.1	0.1
S_{orw}	0.4	0.3	0.15	0.05
k_{rw}^{max}	0.1	0.2	0.5	0.95
n_w	2	2	8	1.5
k_{ro}^{max}	1	1	1	1
n_o	1	1.5	2.5	4
p_c^{max} (kPa)	150	150	150	150
n_c^+	2	1.7	2	\emptyset
p_c^{min} (kPa)	0	-50	-100	-150
n_c^-	\emptyset	1.5	2.5	3
S^*	0.6	0.55	0.5	0.1
p_e (kPa)	1	1	1	1
n_c^{dr}	2	2	2	2

Equations 15 and 16 are used for capillary pressures for drainage and waterflooding, respectively, while using Eqs. 17 and 18 for water and oil relative permeabilities, respectively. (Modified from Blunt (2017))

Table 2 Base parameters used in the J-function calculations

k_b, m^2	1×10^{-13}
ϕ_b , fraction	0.25
$\sigma_{wo} \cos \theta_{wo}$, N/m	3×10^{-2}

$$p_c(S_w) = \begin{cases} p_c^{max} \left(1 - \frac{S_w - S_{wir}}{S^* - S_{wir}} \right)^{n_c^+}, & S_w \in [S_{wir}, S^*] \\ p_c^{min} \left(\frac{S_w - S^*}{1 - S^* - S_{orw}} \right)^{n_c^-}, & S_w \in [S^*, 1 - S_{orw}] \end{cases} \tag{16}$$

$$k_{rw}(S_w) = \begin{cases} k_{rw}^{max} \left(\frac{S_w - S_{wir}}{1 - S_{wir} - S_{orw}} \right)^{n_w}, & S_w \in [S_{wir}, 1 - S_{orw}] \\ \emptyset, & S_w \notin [S_{wir}, 1 - S_{orw}] \end{cases} \tag{17}$$

$$k_{ro}(S_w) = \begin{cases} k_{ro}^{max} \left(1 - \frac{S_w - S_{wir}}{1 - S_{wir} - S_{orw}} \right)^{n_o}, & S_w \in [S_{wir}, 1 - S_{orw}] \\ \emptyset, & S_w \notin [S_{wir}, 1 - S_{orw}] \end{cases} \tag{18}$$

where Eqs. 15 and 16 are used for capillary pressures for drainage $p_c^{dr}(S_w)$ and waterflooding $p_c(S_w)$, respectively, while Eqs. 17 and 18 are used for water $k_{rw}(S_w)$ and oil $k_{ro}(S_w)$ relative permeabilities, respectively; p_c^{max} is the maximum capillary pressure in Pa, p_c^{min} is the minimum capillary pressure in Pa, p_e is the entry pressure in Pa, S^* is the water saturation specified at zero capillary pressure, n_c^{dr} is the exponent used in the drainage capillary pressure, n_c^+ and n_c^- are the exponents used in the positive and negative regions of the capillary pressure for waterflooding, respectively, n_w and n_o are the exponents used in the relative permeability functions for water and oil, respectively, k_{rw}^{max} is the maximum relative permeability to water, and k_{ro}^{max} is the maximum relative permeability to oil. J-function scaling Leverett (1941) is used to correlate capillary pressures with rock properties, resulting in the following expression:

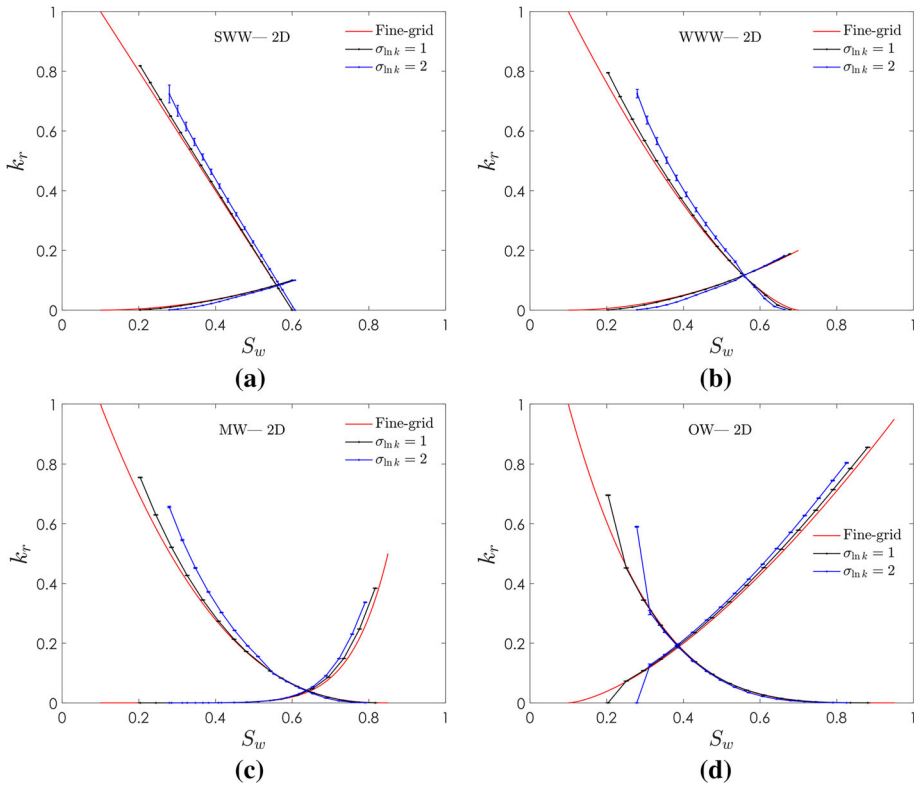


Fig. 11 Upscaled relative permeabilities in 2D for capillary-controlled displacements including the impact of percolation for different wettability states and permeability distributions with $\sigma_{lnk} = \{1, 2\}$. **a** k_r data in strongly water-wet; **b** weakly water-wet; **c** mixed-wet; and **d** oil-wet systems. The original fine-grid k_r curves are also included for comparison purposes. The curves are plotted using average values from five simulations, while the bars represent their standard deviations

$$p_{c_i}(S_w) = \frac{\sqrt{k_b/\phi_b}}{\sqrt{k_i/\phi_i}} p_{c_b}(S_w) \tag{19}$$

where p_{c_i} is the capillary pressure at cell i in Pa, p_{c_b} is a base capillary pressure measured in the laboratory in Pa, k_i and ϕ_i are absolute permeability and porosity in cell i in m^2 and fraction, respectively, and k_b and ϕ_b are base permeability and porosity, respectively.

All model parameters for multiphase flow calculations are listed in Table 1, while Table 2 lists the base parameters used in the J-function calculations, for both drainage and water-flooding. The parameters k_b and ϕ_b are used as a reference for the J-function calculations. In a normal practice, these values are obtained from the same rock where the capillary pressure measurements p_{c_b} were taken from. The main purpose of the J-function scaling is to extrapolate capillary pressure information for systems with known basic properties, e.g. k_i and ϕ_i , for which capillary pressure data are originally unknown. For each wettability state, Eq. 19 is applied to generate a capillary pressure curve in each and every cell in our simulation model.

We now perform simulations to determine average quantities as previously described. For each wetting state, five simulations are performed for each σ_{lnk} . The computations of average relative permeabilities are performed at 16 capillary equilibrium states. The percolation simulations, on the other hand, are performed at a much more refined p_c^{level} distribution,

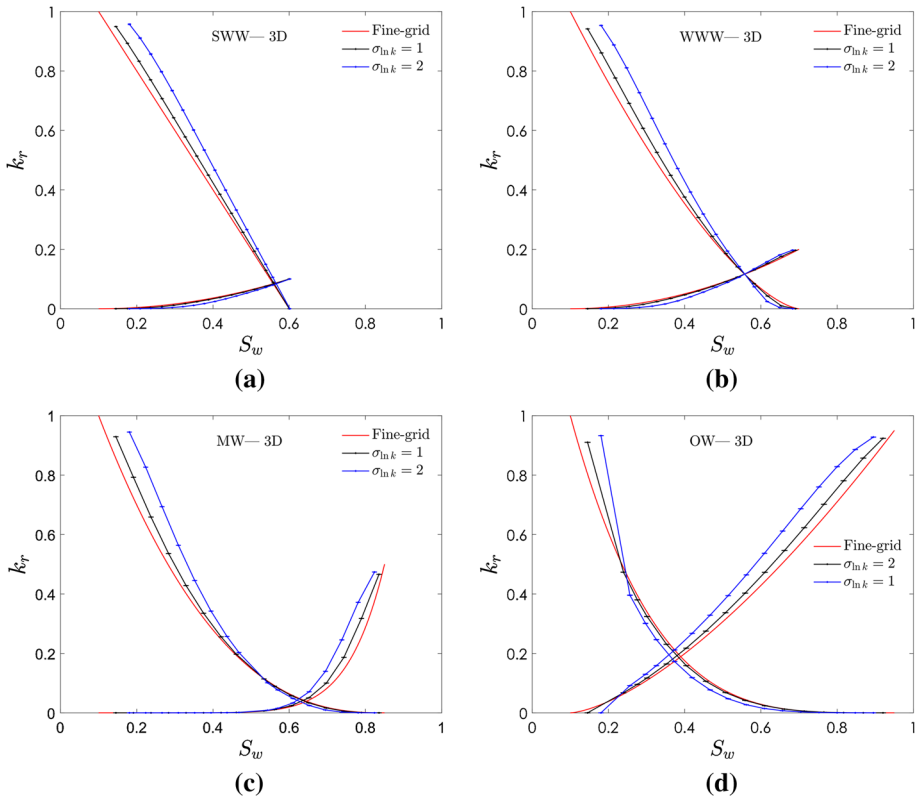


Fig. 12 Upscaled relative permeabilities in 3D for capillary-controlled displacements including the impact of percolation for different wettability states and permeability distributions with $\sigma_{ln,k} = \{1, 2\}$. **a** k_r curves in strongly water-wet; **b** weakly water-wet; **c** mixed-wet; and **d** oil-wet systems. Original k_r curves are also included for comparison purposes. The curves are plotted using average values from five simulations, while the bars represent their standard deviations

estimated from p_c^{\max} and p_c^{\min} , to identify accurately trapping, from which average water saturations are determined. The elements of p_c^{\max} and p_c^{\min} distributions can be calculated from Eq. 19 as follows:

$$p_{c_i}^{\max} = \frac{\sqrt{k_b/\phi_b}}{\sqrt{k_i/\phi_i}} p_c^{\max} \tag{20}$$

$$p_{c_i}^{\min} = \frac{\sqrt{k_b/\phi_b}}{\sqrt{k_i/\phi_i}} p_c^{\min} \tag{21}$$

where $p_{c_i}^{\max}$ and $p_{c_i}^{\min}$ are the maximum and minimum capillary pressures at cell i , p_c^{\max} and p_c^{\min} are given for all wetting conditions in Table 1. Other parameters are defined previously in Eq. 19. Repeated elements are removed from the distributions and sorted. The p_c^{level} distribution is then estimated by computing percentiles at every half a percentage point.

Figures 11 and 12 show the upscaled relative permeabilities for $\sigma_{ln,k} = \{1, 2\}$, for 2D and 3D, respectively. Each curve represents the overall average of the five simulations, while the bars indicate their standard deviations. We can observe, in general, that as $\sigma_{ln,k}$ increases, the deviations of both \tilde{k}_{rw} and \tilde{k}_{ro} from the fine-grid functions become more apparent. It is also

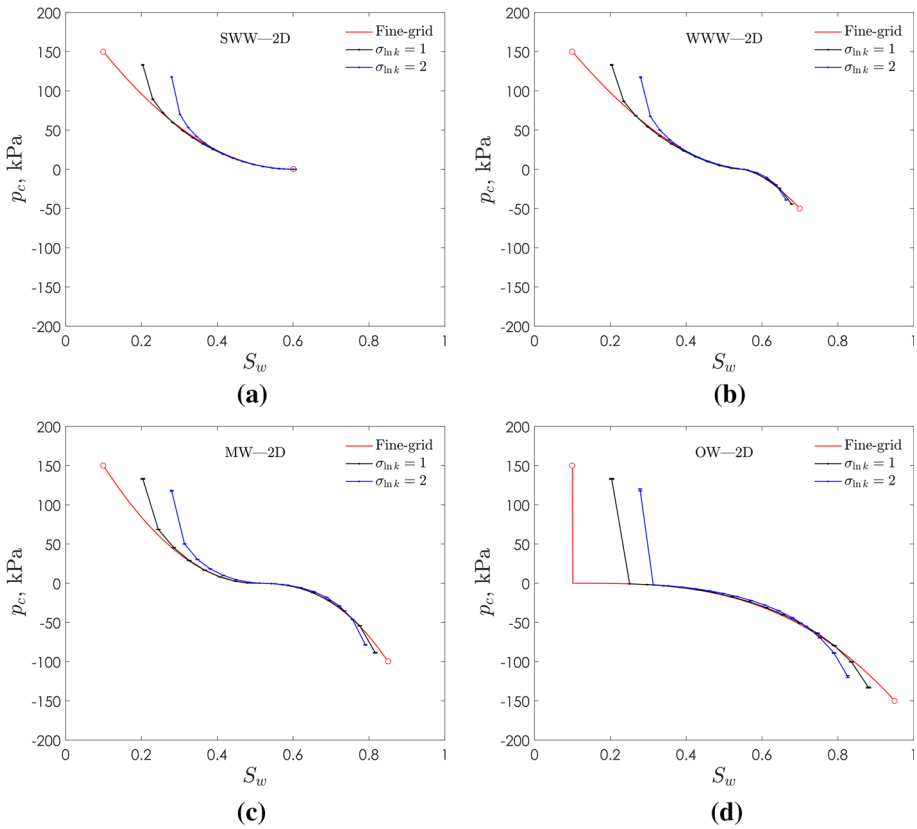


Fig. 13 Upscaled capillary pressures in 2D for capillary-controlled displacements for different wettability states and permeability distributions with $\sigma_{\ln k} = \{1, 2\}$. **a** p_c curves in strongly water-wet; **b** weakly water-wet; **c** mixed-wet; and **d** oil-wet media. Original p_c curves are also included for comparison purposes. The curves are plotted using average values from five simulations, while the bars represent their standard deviations

shown that the trapping of fluids also increases with $\sigma_{\ln k}$, though the trapping in 2D is larger than in 3D. We also see in Fig. 11 that the maximum value of \tilde{k}_{rw} and \tilde{k}_{ro} decreases with more trapping, indicating that the additional trapped fluids preferentially fill some regions of the domain that have some contribution to the overall permeability; this is only true for 2D. In 3D, however, this is not observed (Fig. 12), suggesting that the additional trapped fluids occupy regions that do not contribute to the overall permeability of the sample.

The averaged water relative permeabilities are only finite once the water percolates across the system, which occurs at a finite occupancy. We see an increase in the minimum water saturation at which water flows across the domain. At the end of primary drainage, water is trapped at the large scale in isolated clusters distributed across the whole domain. As water is injected into the system, these clusters reconnect increasing the averaged water relative permeabilities more rapidly.

It is demonstrated that \tilde{k}_{ro} generally increases over a wide range of \tilde{S}_w as $\sigma_{\ln k}$ increases, especially for SWW, WWW and MW media. This indicates that water preferentially resides in the lower permeability rock at a given \tilde{S}_w . Similarly for \tilde{k}_{rw} in MW and OW systems,

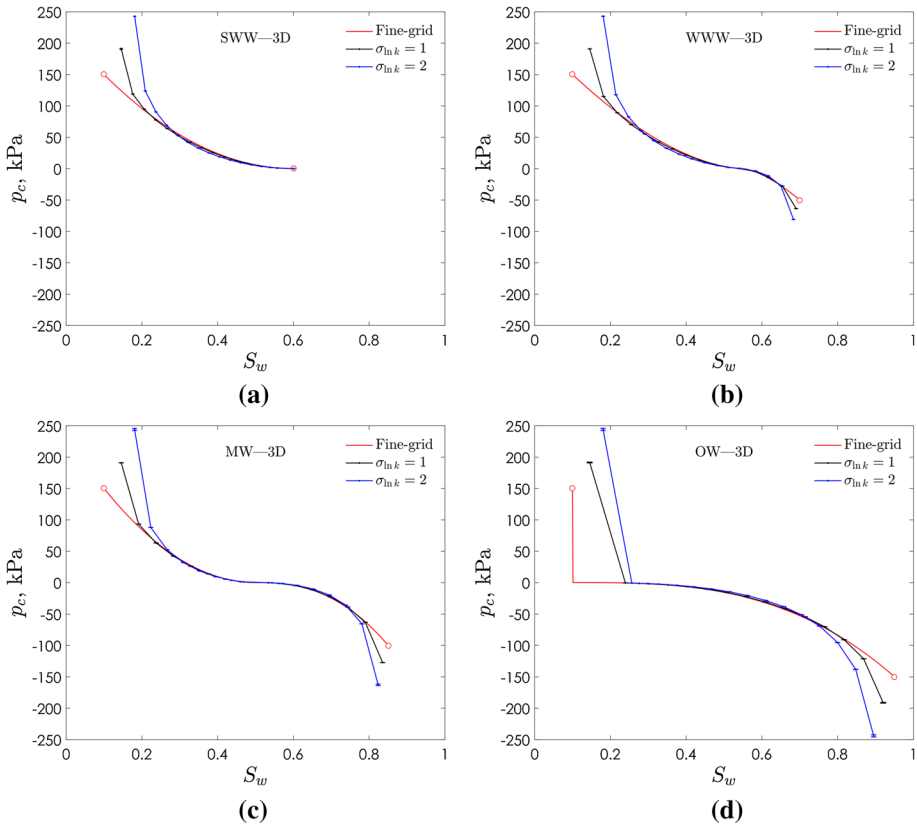


Fig. 14 Upscaled capillary pressures in 3D for capillary-controlled displacements for different wettability states and permeability distributions with $\sigma_{lnk} = \{1, 2\}$. **a** p_c curves in strongly water-wet; **b** weakly water-wet; **c** mixed-wet; and **d** oil-wet media. Original p_c curves are also included for comparison purposes. The curves are plotted using average values from five simulations, while the bars represent their standard deviations

where it generally increases for the late values of \tilde{S}_w as σ_{lnk} increases, suggesting that the remaining oil now tends to occupy the lower permeability portions of the system.

Average capillary pressures are shown in Figs. 13 and 14 for 2D and 3D models, respectively. In general, little sensitivity is observed on the trends of the curves for all the wetting states and permeability distributions, except near the end-point saturations. What is observed is the trapping of fluids as shown in the figures and listed in Tables 3 and 4, for 2D and 3D systems, respectively. These values reported in the table are derived from the distributions generated from the five simulation runs. The symbols \tilde{S}_{wir} and \tilde{S}_{orw} are used to refer to the upscaled irreducible water and residual oil saturations, respectively, while $|\Delta S_{wir}|$ and $|\Delta S_{orw}|$ show the absolute difference between the upscaled quantities and the fine-grid inputs. As can be seen that more fluids are trapped at the Darcy scale as σ_{lnk} increases.

We observe also that the trapping of water \tilde{S}_{wir} does not vary between the different wetting states, but with σ_{lnk} and the dimensionality of the system. This is because the capillary pressure function defined for drainage being the same for all the wetting states. On average, about 10% of the water is trapped at the large scale in 2D for $\sigma_{lnk} = 1$, and 18% for $\sigma_{lnk} = 2$, while about half of that is seen in 3D.

Table 3 Upscaled end-point saturations for the 2D model (1 million grid cells)

	\tilde{S}_{wir}	\tilde{S}_{orw}	$ \Delta S_{wir} $	$ \Delta S_{orw} $
SWW				
$\sigma_{lnk} = 1$	0.2036 ± 0.0013	0.4000 ± 0.0000	0.1036 ± 0.0013	0.0000 ± 0.0000
$\sigma_{lnk} = 2$	0.2797 ± 0.0004	0.3928 ± 0.0001	0.1797 ± 0.0004	0.0072 ± 0.0001
WWW				
$\sigma_{lnk} = 1$	0.2036 ± 0.0004	0.3221 ± 0.0005	0.1036 ± 0.0004	0.0221 ± 0.0005
$\sigma_{lnk} = 2$	0.2798 ± 0.0008	0.3368 ± 0.0006	0.1798 ± 0.0008	0.0368 ± 0.0006
MW				
$\sigma_{lnk} = 1$	0.2036 ± 0.0013	0.1835 ± 0.0006	0.1036 ± 0.0013	0.0335 ± 0.0006
$\sigma_{lnk} = 2$	0.2796 ± 0.0016	0.2094 ± 0.0007	0.1796 ± 0.0016	0.0594 ± 0.0007
OW				
$\sigma_{lnk} = 1$	0.2036 ± 0.0011	0.1191 ± 0.0014	0.1036 ± 0.0011	0.0691 ± 0.0014
$\sigma_{lnk} = 2$	0.2785 ± 0.0021	0.1741 ± 0.0029	0.1785 ± 0.0021	0.1241 ± 0.0029

$|\Delta S_{wir}|$ and $|\Delta S_{orw}|$ refer to the absolute difference between the upscaled quantities and the fine-grid inputs

Table 4 Upscaled end-point saturations for the 3D model (8 million grid cells)

	\tilde{S}_{wir}	\tilde{S}_{orw}	$ \Delta S_{wir} $	$ \Delta S_{orw} $
SWW				
$\sigma_{lnk} = 1$	0.1454 ± 0.0002	0.4000 ± 0.0000	0.0454 ± 0.0002	0.0000 ± 0.0000
$\sigma_{lnk} = 2$	0.1808 ± 0.0003	0.3984 ± 0.0000	0.0808 ± 0.0003	0.0016 ± 0.0000
WWW				
$\sigma_{lnk} = 1$	0.1454 ± 0.0001	0.3097 ± 0.0000	0.0454 ± 0.0001	0.0097 ± 0.0000
$\sigma_{lnk} = 2$	0.1808 ± 0.0001	0.3167 ± 0.0000	0.0808 ± 0.0001	0.0167 ± 0.0000
MW				
$\sigma_{lnk} = 1$	0.1454 ± 0.0001	0.1645 ± 0.0000	0.0454 ± 0.0001	0.0145 ± 0.0000
$\sigma_{lnk} = 2$	0.1807 ± 0.0003	0.1763 ± 0.0003	0.0807 ± 0.0003	0.0263 ± 0.0003
OW				
$\sigma_{lnk} = 1$	0.1454 ± 0.0001	0.0798 ± 0.0003	0.0454 ± 0.0001	0.0298 ± 0.0003
$\sigma_{lnk} = 2$	0.1805 ± 0.0002	0.1049 ± 0.0004	0.0805 ± 0.0002	0.0549 ± 0.0004

$|\Delta S_{wir}|$ and $|\Delta S_{orw}|$ are the absolute difference between the upscaled quantities and the fine-grid inputs

For the large-scale trapping of oil, we observe different behaviours than water between the wetting conditions, influenced by the capillary pressure functions for waterflooding. Here, the highest trapping happens in oil-wet media at 12% and 5% in 2D and 3D, respectively, at $\sigma_{lnk} = 2$. This trapping is *in addition* to the pore-scale trapping, given by S_{orw} in Table 1.

10 Conclusions

A modified upscaling procedure for steady-state capillary-controlled immiscible displacements is proposed, which accounts for the large-scale connectivity in Darcy-scale simulations. The key idea is that at a given capillary equilibrium state, some regions in the system may

form disconnected clusters preventing global connectivity. To tackle such displacements, a revised steady-state upscaling algorithm is introduced accounting for the trapping of fluids in a large-scale invasion percolation displacement. The process is explained through illustrative examples, in which four different wettability states are studied—strongly water-wet, weakly water-wet, mixed-wet and oil-wet. It is observed that, at Darcy scale, the capillary trapping for water increases in heterogeneous media and is influenced mainly by the capillary pressure function defined for drainage. For the large-scale trapping of oil, we observe different behaviours between the wetting conditions, controlled by the capillary pressure functions for waterflooding, in which the highest trapping is observed in oil-wet systems.

The analysis of this paper could be extended in future studies to explore the impact of viscous forces, using realistic geology, and including the effects of hysteresis in the multiphase flow functions.

Acknowledgements The first author would like to thank Saudi Aramco for their generous financial support towards his PhD at Imperial College London.

Open Access This article is distributed under the terms of the Creative Commons Attribution 4.0 International License (<http://creativecommons.org/licenses/by/4.0/>), which permits unrestricted use, distribution, and reproduction in any medium, provided you give appropriate credit to the original author(s) and the source, provide a link to the Creative Commons license, and indicate if changes were made.

References

- Barker, J.W., Dupouy, P.: An analysis of dynamic pseudo-relative permeability methods for oil-water flows. *Petrol. Geosci.* **5**(4), 385–394 (1999)
- Barker, J.W., Thibeau, S.: A critical review of the use of pseudorelative permeabilities for upscaling. *SPE J.* **12**(2), 138–143 (1997)
- Blunt, M.J.: *Multiphase Flow in Permeable Media: a Pore-Cscale Perspective*. Cambridge University Press, Cambridge (2017)
- Braun, E.M., Blackwell, R.J.: A steady-state technique for measuring oil-water relative permeability curves at reservoir conditions. In: *SPE Annual Technical Conference and Exhibition*, SPE-10155-MS, pp. 1–10 (1981)
- Coll, C., Muggenridge, A.H., Jing, X.D.: Regional upscaling: a new method to upscale waterflooding in heterogeneous reservoirs for a range of capillary and gravity effects. *SPE J.* **6**(3), 299–310 (2001)
- Deng, Y., Blöte, H.W.J.: Monte Carlo study of the site-percolation model in two and three dimensions. *Phys. Rev. E* **72**(1), 016126 (2005)
- Durlofsky, L.J.: Use of higher moments for the description of upscaled, process independent relative permeabilities. *SPE J.* **2**(4), 474–484 (1997)
- Ekrann, S., Aasen, J.O.: Steady-state upscaling. *Transp. Porous Media* **41**(3), 245–262 (2000)
- Grimmett, G.: What is Percolation?. In: *Percolation*. Springer, Berlin, pp. 1–31 (1999)
- Guzman, R.E., Giordano, D., Fayers, F.J., Godi, A., Aziz, K.: Evaluation of dynamic pseudofunctions for reservoir simulation. *SPE J.* **4**(1), 37–46 (1999)
- Hilden, S.T., Berg, C.F.: An analysis of unsteady flooding processes: varying force balance and the applicability of steady-state upscaling. *Transp. Porous Media* **115**(1), 125–152 (2016)
- Honarpour, M., Mahmood, S.M.: Relative-permeability measurements: an overview. *J. Petrol. Technol.* **40**(8), 963–966 (1988)
- Hunt, A., Ewing, R., Ghanbarian, B.: *Percolation Theory for Flow in Porous Media*, 880th edn. Springer, Berlin (2014)
- Ioannidis, M.A., Chatzis, I., Sudicky, E.A.: The effect of spatial correlations on the accessibility characteristics of three-dimensional cubic networks as related to drainage displacements in porous media. *Water Resour. Res.* **29**(6), 1777–1785 (1993)
- Ioannidis, M.A., Chatzis, I., Dullin, A.L.: Macroscopic percolation model of immiscible displacement: effects of buoyancy and spatial structure. *Water Resour. Res.* **32**(11), 3297–3310 (1996)
- Jacks, H.H., Smith, O.J.E., Mattax, C.C.: The modeling of a three-dimensional reservoir with a two-dimensional reservoir simulator—the use of dynamic pseudo functions. *SPE J.* **13**(3), 175–185 (1973)

- Jacobsen, J.L.: Critical points of Potts and O (N) models from eigenvalue identities in periodic temperley-lieb algebras. *J. Phys. A Math. Theor.* **48**(45), 454003–454033 (2015)
- Johnson, E.F., Bossler, D.P., Bossler, V.O.N.: Calculation of relative permeability from displacement experiments. *Trans. AIME* **207**, 370–372 (1959)
- Jones, S.C., Roszelle, W.O.: Graphical techniques for determining relative permeability from displacement experiments. *J. Petrol. Technol.* **30**(5), 807–817 (1978)
- Jonoud, S., Jackson, M.D.: New criteria for the validity of steady-state upscaling. *Transp. Porous Media* **71**(1), 53–73 (2008a)
- Jonoud, S., Jackson, M.D.: Validity of steady-state upscaling techniques. *SPE J.* **11**(2), 405–416 (2008b)
- Juanes, R., Spiteri, E.J., Orr Jr., F.M., Blunt, M.J.: Impact of relative permeability hysteresis on geological CO₂ storage. *Water Resour. Res.* **42**, 1–13 (2006)
- King, P.R.: The use of renormalization for calculating effective permeability. *Transp. Porous Media* **4**(1), 37–58 (1989)
- King, P.R., Muggeridge, A.H., Price, W.G.: Renormalization calculations of immiscible flow. *Transp. Porous Media* **12**(3), 237–260 (1993)
- Kueper, B.H., McWhorter, D.B.: The use of macroscopic percolation theory to construct large-scale capillary pressure curves. *Water Resour. Res.* **28**(9), 2425–2436 (1992)
- Kumar, A.T.A., Jerauld, G.R.: Impacts of scale-up on fluid flow from plug to Gridblock scale in reservoir rock. In: *SPE/DOE Tenth Symposium on Improved Oil Recovery*, SPE-35452-MS, pp. 1–16 (1996)
- Kyte, J.R., Berry, D.W.: New pseudo functions to control numerical dispersion. *SPE J.* **15**(4), 269–276 (1975)
- Lee, M.J.: Complementary algorithms for graphs and percolation. *Phys. Rev. E* **76**(2), 027702 (2007)
- Leverett, M.: Capillary behavior in porous solids. *Trans. AIME* **141**(1), 152–169 (1941)
- Lohne, A., Virnovsky, G.A., Durlafsky, L.J.: Two-stage upscaling of two-phase flow: from core to simulation scale. *SPE J.* **11**(3), 304–316 (2006)
- Muskat, M.: The flow of fluids through porous media. *J. Appl. Phys.* **8**(4), 274–282 (1937)
- Newman, M.E.J., Ziff, R.M.: Efficient Monte Carlo algorithm and high-precision results for percolation. *Phys. Rev. Lett.* **85**(19), 4104–4107 (2000)
- Odsæter, L.H., Berg, C.F., Rustad, A.B.: Rate dependency in steady-state upscaling. *Transp. Porous Media* **110**(3), 565–589 (2015)
- Osoba, J.S., Richardson, J.G., Kerver, J.K., Hafford, J.A., Blair, P.M.: Laboratory measurements of relative permeability. *J. Petrol. Technol.* **3**(2), 47–56 (1951)
- Pickup, G.E., Stephen, K.D.: Steady-state scale-up methods. In: *6th European Conference on the Mathematics of Oil Recovery*, Peebles, Scotland, pp. 8–11 (1998)
- Pickup, G.E., Sorbie, K.S.: The scaleup of two-phase flow in porous media using phase permeability tensors. *SPE J.* **1**(4), 369–381 (1996)
- Richardson, J.G., Kerver, J.K., Hafford, J.A., Osoba, J.S.: Laboratory determination of relative permeability. *J. Petrol. Technol.* **4**(8), 187–196 (1952)
- Saad, N., Cullick, A.S., Honarpour, M.M.: Effective relative permeability in scale-up and simulation. In: *Proceedings of SPE Rocky Mountain Regional/Low-Permeability Reservoirs Symposium*, SPE-29592, pp. 451–464 (1995)
- Saadatpoor, E., Bryant, S.L., Sepehrmoori, K.: New trapping mechanism in carbon sequestration. *Transp. Porous Media* **82**(1), 3–17 (2010)
- Škvor, J., Nezbeda, I.: Percolation threshold parameters of fluids. *Phys. Rev. E* **79**(4), 041141 (2009)
- Stephen, K.D., Pickup, G.E.: Steady state solutions of immiscible two-phase flow in strongly heterogeneous media: implications for upscaling. In: *SPE Reservoir Simulation Symposium*, SPE-51912-MS, pp. 1–2 (1999)
- Stephen, K.D., Pickup, G.E., Sorbie, K.S.: The local analysis of changing force balances in immiscible incompressible two-phase flow. *Transp. Porous Media* **45**(1), 63–88 (2001)
- Stone, H.L.: Rigorous black oil pseudo functions. In: *SPE Reservoir Simulation Symposium*, SPE-21207, pp. 1–12 (1991)
- Valvatne, P.H., Blunt, M.J.: Predictive pore-scale modeling of two-phase flow in mixed wet media. *Water Resour. Res.* **40**(7), 1–20 (2004)
- Virnovsky, G.A., Friis, H.A., Lohne, A.: A steady-state upscaling approach for immiscible two-phase flow. *Transp. Porous Media* **54**(2), 167–192 (2004)
- Wallstrom, T.C., Christie, M.A., Durlafsky, L.J., Sharp, D.H.: Effective flux boundary conditions for upscaling porous media equations. *Transp. Porous Media* **46**(2), 139–153 (2002)
- West, D.B.: *Introduction to Graph Theory*, 2nd edn. Prentice hall, Upper Saddle River (2001)
- Xu, X., Wang, J., Lv, J.P., Deng, Y.: Simultaneous analysis of three-dimensional percolation models. *Front. Phys.* **9**(1), 113–119 (2014)

- Yortsos, Y.C., Satik, C., Salin, D., Bacri, J.C.: Large-scale averaging of drainage at local capillary control. In: Proceedings of SPE Annual Fall Meeting, SPE-22592, pp. 55–70 (1991)
- Yortsos, Y.C., Satik, C., Bacri, J.C., Salin, D.: Large-scale percolation theory of drainage. *Transp. Porous Media* **10**(2), 171–195 (1993)